INTERNATIONAL JOURNAL FOR NUMERICAL METHODS IN FLUIDS
Int. J. Numer. Meth. Fluids 2001; **37**: 657–689 (DOI: 10.1002/fld.187)

Numerical simulation of high-Reynolds number flow around circular cylinders by a three-step FEM–BEM model

D. L. Young*[,1], J. L. Huang and T. I. Eldho

Department of Civil Engineering and Hydrotech Research Institute, National Taiwan University, Taipei, Taiwan, ROC

SUMMARY

An innovative computational model, developed to simulate high-Reynolds number flow past circular cylinders in two-dimensional incompressible viscous flows in external flow fields is described in this paper. The model, based on transient Navier–Stokes equations, can solve the infinite boundary value problems by extracting the boundary effects on a specified finite computational domain, using the projection method. The pressure is assumed to be zero at infinite boundary and the external flow field is simulated using a direct boundary element method (BEM) by solving a pressure Poisson equation. A three-step finite element method (FEM) is used to solve the momentum equations of the flow. The present model is applied to simulate high-Reynolds number flow past a single circular cylinder and flow past two cylinders in which one acts as a control cylinder. The simulation results are compared with experimental data and other numerical models and are found to be feasible and satisfactory. Copyright © 2001 John Wiley & Sons, Ltd.

KEY WORDS: boundary elements; finite elements; incompressible viscous flow; Navier–Stokes equations; vortex shedding suppression

1. INTRODUCTION

The vortex shedding phenomena from bluff bodies like circular cylinders are commonly considered as the main source that causes the flow induced vibrations, noises, and even collapse of a body in an external flow. The study of the vortex shedding over a circular cylinder and suppression of fluid forces has received much attention, since practical applications are expected in various areas of engineering such as high-rise buildings analysis, wind engineering, aeronautics, etc. The major difficulty in simulating the vortex shedding and fluid force on the bluff bodies in external flow fields lies in setting the boundary conditions of the computational domain to simulate the external flow that has infinite domain.

* Correspondence to: Department of Civil Engineering, National Taiwan University, Taipei, Taiwan 10617, ROC.
[1] E-mail: dlyoung@hy.ntu.edu.tw

Copyright © 2001 John Wiley & Sons, Ltd.

Received July 2000
Accepted February 2001

Even though a large number of experimental studies have been reported on laminar vortex shedding flows (for example, Reference [1]) at low Reynolds number, investigations in unsteady flow field at high Reynolds number are rather limited due to the difficulties involved in unsteady flow measurements, with rare exceptions such as the works of Cantwell and Coles [2] and Sakamato and Haniu [3]. Many methods have been developed to suppress vortex shedding and to reduce the fluid forces over circular cylinders [4]. Recently, Strykowsky and Sreenivasan [1] reported that vortex shedding can be suppressed by introducing small diameter control cylinders at a low Reynolds number flow regime, and Sakamato and Haniu [3] succeeded in reducing the fluid forces acting on a circular cylinder at comparatively large Reynolds numbers with the introduction of a control cylinder near the main cylinder. The aim of the present work is the numerical investigation of the flow around a main cylinder and the reduction of the fluid forces around the main cylinder by introducing a control cylinder at various positions, using an innovative numerical scheme.

Numerical simulations of vortex shedding flow past bluff bodies have been performed by many researchers with the use of the finite volume method (FVM), finite difference method (FDM), finite element method (FEM) or the boundary element method (BEM). Braza *et al.* [5] and Franke *et al.* [6] used the FVM and analyzed the vortex shedding past circular cylinders and square cylinders in a laminar flow regime. Using FDM, Lecointe and Piquet [7] calculated the flow around circular cylinders using the stream function–vorticity approach. A Galerkin FEM has been used by Jackson [8] to study vortex shedding in flow past variously shaped bodies by solving steady state equations. FEM and BEM have been widely in use for the solution of various fluid dynamics problems in the last two decades. For the solution of different forms of Navier–Stokes equations, the use of FEM [9,10] and BEM [11] has been described by various researches.

In FEM, it is well known that the conventional Galerkin finite element scheme leads to spurious oscillatory solutions for fluid dynamics problems at high Reynolds numbers. To overcome such oscillation and numerical dissipation, various upwind schemes have been successfully presented by researchers. In the finite element approximation, the upwind schemes have been developed by the use of schemes based on the Petrov–Galerkin [12–14] or the Taylor–Galerkin methods [15]. Jiang and Kawahara [16] recently developed a three-step finite element scheme for the unsteady incompressible viscous flows, based on the Taylor–Galerkin schemes.

In this paper, a new computational model is presented to solve the high-Reynolds number flow past bluff bodies in external flow fields. The model, based on transient Navier–Stokes equations, can solve the infinite boundary value problems by extracting the boundary effects on a specified finite computational domain, using the projection method [17]. A three-step FEM is used to solve the momentum equations of the flow. The pressure Poisson equation for the external flow field is treated by the BEM and then coupled with the three-step FEM scheme. The feasibility of the developed numerical scheme in the application of high-Reynolds number flows has been illustrated by applying the model to simulate high-Reynolds number flow past a single circular cylinder, and flow past two cylinders in which one acts as a control cylinder. The simulation results are compared with some experimental data and other numerical models and are found to be feasible and satisfactory.

Copyright © 2001 John Wiley & Sons, Ltd.

After presenting the governing equations, the numerical formulation using coupled BEM and three-step FEM are briefly described. Then the solution procedure and numerical results for two case studies of high-Reynolds number flow around a single circular cylinder and flow around two cylinders in which one acts as a control cylinder, are presented and followed by a few concluding remarks.

2. GOVERNING EQUATIONS

The governing equations of the motion of an incompressible viscous fluid flow can be expressed by the Navier–Stokes equations and continuity equation and written in Cartesian tensor notation as follows:

$$\frac{\partial u_i}{\partial x_i} = 0 \tag{1}$$

$$\frac{\partial u_i}{\partial t} + \frac{u_j \, \partial u_i}{\partial x_j} = -\frac{1}{\rho}\frac{\partial p}{\partial x_i} + \nu \frac{\partial^2 u_i}{\partial x_j \, \partial x_j} + f_i \tag{2}$$

where u_i, $i = 1, 2$, are two components of the velocity vector in the x-, y-directions, p is pressure, ν is kinematic viscosity, t is time, ρ is mass density, $f_i = \rho g l_i$ are body forces in the x-, y-directions, g is gravitational acceleration and l_i are direction cosines in the x- and y-directions. Using the following dimensionless forms of the variables:

$$x^* = x/D, \quad y^* = y/D, \quad u^* = u/u_0, \quad v^* = v/u_0, \quad t^* = tu_0/D, \quad p^* = p/\rho u_0^2 \tag{3}$$

where D is a characteristic length and u_0 is a characteristic velocity. Now Equations (1) and (2) can be written as

$$\frac{\partial u_i^*}{\partial x_i^*} = 0 \tag{4}$$

$$\frac{\partial u_i^*}{\partial t^*} + \frac{u_j^* \, \partial u_i^*}{\partial x_j^*} = -\frac{\partial p^*}{\partial x_i^*} + \frac{1}{Re}\frac{\partial^2 u_i^*}{\partial x_j^* \, \partial x_j^*} + \frac{l_i}{Fr^2} \tag{5}$$

where $Re = u_0 D/\nu$ is the Reynolds number and $Fr = u_0/(gD)^{1/2}$ is the Froude number. Dropping the asterisk from the dimensionless variables in the following equations for brevity and putting the body force terms into the pressure field for neglecting the free surface effects, the non-dimensionalized governing equations for (1) and (2) can be written as

$$\frac{\partial u_i}{\partial x_i} = 0 \tag{6}$$

Copyright © 2001 John Wiley & Sons, Ltd.

$$\frac{\partial u_i}{\partial t} + \frac{u_j \partial u_i}{\partial x_j} = -\frac{\partial p}{\partial x_i} + \frac{1}{Re}\left(\frac{\partial^2 u_i}{\partial x_j \partial x_j}\right) \tag{7}$$

Generally used boundary conditions are the prescribed velocities

$$u = u_0, \qquad v = v_0 \tag{8}$$

and the non-slip boundary conditions. At the initial time, some known values of velocities and pressure can be prescribed as initial conditions.

As far as external flows are concerned, the outer boundaries are located at the infinity. In numerical computations, due to the limitations of computational facilities, it is assumed that the computational domain is limited to the finite region. In the present analysis we assume that

$$\nabla^2 p = 0 \tag{9}$$

is valid out of the finite computational domain. As a consequence, only the inflow boundary condition is needed as the boundary requirement of the computational domain. A sample computational domain for the type of problem that will be considered in the present study is shown in Figure 1 with boundary conditions. The boundary condition of the fixed body in the flow is set as a no-slip boundary.

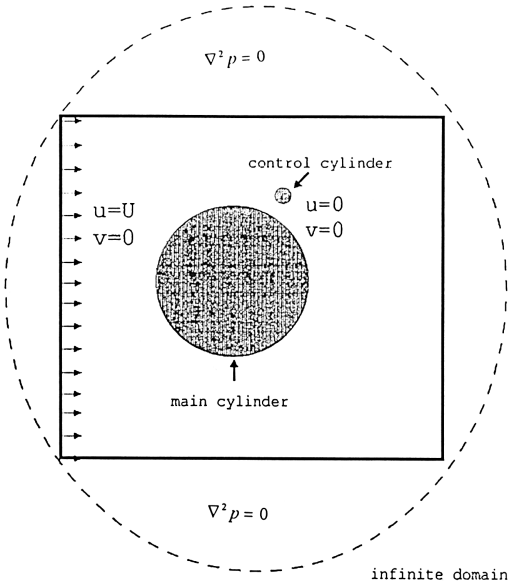

Figure 1. Computational domain and boundary conditions for a typical problem.

Copyright © 2001 John Wiley & Sons, Ltd.

3. NUMERICAL FORMULATION

As mentioned earlier, in the present model, a coupled three-step FEM–BEM approach is used in the solution of the governing differential equations. In this section, the numerical formulation is briefly described.

3.1. Three-step FEM formulation for momentum equations

In the present model, the mass–momentum Navier–Stokes equations are approximated using an explicit three-step FEM based on a Taylor series expansion in time [16]. From Taylor's series, a function h in time can be represented as

$$h(t+\Delta t) = h(t) + \Delta t \frac{\partial h(t)}{\partial t} + \frac{\Delta t^2}{2}\frac{\partial^2 h(t)}{\partial t^2} + \frac{\Delta t^3}{6}\frac{\partial^3 h(t)}{\partial t^3} + O(\Delta t^4) \tag{10}$$

Approximating Equation (10) up to third-order accuracy, the three-step formulation can be written as

$$h\left(t+\frac{\Delta t}{3}\right) = h(t) + \frac{\Delta t}{3}\frac{\partial h(t)}{\partial t} \tag{11}$$

$$h\left(t+\frac{\Delta t}{2}\right) = h(t) + \frac{\Delta t}{2}\frac{\partial h(t+\Delta t/3)}{\partial t} \tag{12}$$

$$h(t+\Delta t) = h(t) + \Delta t \frac{\partial h(t+\Delta t/2)}{\partial t} \tag{13}$$

When Equations (11)–(13) are discretized using the standard Galerkin FEM and the resulting finite element equations are solved using the Jacobian iteration, the three-step FEM is obtained [16]. This method has all the advantages of the Taylor–Galerkin method and is stable while solving the convective transport equations.

From the above scheme, using a projection method of the Navier–Stokes equations [17], one can convert Equation (7) in the following steps:

Step 1

$$\frac{u_i^{n+1/3} - u_i^n}{\Delta t/3} = -u_j^n \frac{\partial u_i^n}{\partial x_j} - \frac{\partial p^n}{\partial x_i} + \frac{1}{Re}\nabla^2 u_i^n \tag{14}$$

Step 2

$$\frac{u_i^{n+1/2} - u_i^n}{\Delta t/2} = -u_j^{n+1/3} \frac{\partial u_i^{n+1/3}}{\partial x_j} - \frac{\partial p^n}{\partial x_i} + \frac{1}{Re}\nabla^2 u_i^{n+1/3} \tag{15}$$

Copyright © 2001 John Wiley & Sons, Ltd.

Step 3

$$\frac{u_i^* - u_i^n}{\Delta t} = -u_j^{n+1/2}\frac{\partial u_i^{n+1/2}}{\partial x_j} + \frac{1}{Re}\nabla^2 u_i^{n+1/2} \tag{16}$$

where u_i^* is the apparent velocity. Combining the continuity equation (6) and taking the gradient of Equation (16), the pressure Poisson equation is derived to correct the velocity equation as

$$\nabla^2 p^{n+1} = \frac{1}{\Delta t}\left(\frac{\partial u_i^*}{\partial x_i}\right) \tag{17}$$

Now the present velocity can be derived as

$$u_i^{n+1} = u_i^* - \Delta t\frac{\partial p^{n+1}}{\partial x_i} \tag{18}$$

Spatial discretization of Equations (14)–(16) are performed by the standard Galerkin method using four-point bilinear elements [9]. The resulting finite element equations can be expressed as

For step 1

$$M_{ij}\frac{\vec{u}_j^{n+1/3} - \vec{u}_j^n}{\Delta t/3} = -A_{ij}^n\vec{u}_j^n - \vec{B}_{ij}p_j^n - \frac{1}{Re}S_{ij}\vec{u}_j^n + \int_{\partial\Omega}\frac{N_i}{Re}\left(\frac{\partial\vec{u}^n}{\partial n}\right)\mathrm{d}S \tag{19}$$

For step 2

$$M_{ij}\frac{\vec{u}_j^{n+1/2} - \vec{u}_j^n}{\Delta t/2} = -A_{ij}^{n+1/3}\vec{u}_j^{n+1/3} - \vec{B}_{ij}p_j^n - \frac{1}{Re}S_{ij}\vec{u}_j^{n+1/3} + \int_{\partial\Omega}\frac{N_i}{Re}\left(\frac{\partial\vec{u}^{n+1/3}}{\partial n}\right)\mathrm{d}S \tag{20}$$

For step 3

$$M_{ij}\frac{\vec{u}_j^* - \vec{u}_j^n}{\Delta t} = -A_{ij}^{n+1/2}\vec{u}_j^{n+1/2} - \frac{1}{Re}S_{ij}\vec{u}_j^{n+1/2} + \int_{\partial\Omega}\frac{N_i}{Re}\left(\frac{\partial\vec{u}^{n+1/2}}{\partial n}\right)\mathrm{d}S \tag{21}$$

Equations (18) can be discretized as

$$M_{ij}\vec{u}_n^{n+1} = M_{ij}\vec{u}_j^* - \Delta t\vec{B}_{ij}p_j^{n+1} \tag{22}$$

where

$$M_{ij} = \int_\Omega N_i N_j\,\mathrm{d}\Omega$$

Copyright © 2001 John Wiley & Sons, Ltd.

$$A_{ij}^{n} = \int_{\Omega} N_i \left(u_k^n \frac{\partial N_j}{\partial x_k} \right) \mathrm{d}\Omega$$

$$\vec{B}_{ij} = \int_{\Omega} N_i \frac{\partial N_j}{\partial x_k} \mathrm{d}\Omega$$

$$S_{ij} = \int_{\Omega} \left(\frac{\partial N_i}{\partial x_k} \frac{\partial N_j}{\partial x_k} \right) \mathrm{d}\Omega$$

in which N_i and N_j are the shape functions and arrows stand for the two components associated with the x- and y-directions.

After assembling the system and applying the boundary conditions, the system of equations are solved using the Jacobian iterative scheme.

3.2. BEM formulation for pressure Poisson equation

Consider the Poisson type pressure equation in p and u_i^*, Equation (17)

$$\nabla^2 p = \frac{1}{\Delta t} \left(\frac{\partial u_i^*}{\partial x_i} \right) = b \tag{23}$$

with pressure boundary conditions as

$$\bar{p} = p_0 \quad \text{on } \Gamma_1, \qquad \bar{q} = \frac{\partial p_o}{\partial n} \quad \text{on } \Gamma_2 \tag{24}$$

where n is the unit outward normal vector. In the present model, an iterative scheme is used such that the velocity u_i^* is known in the current iteration and time step from the previous step by solving the Navier–Stokes equations.

A weighting function p^* can now be introduced such that it has continuous first derivatives within the domain. The following weighted residual statement can now be written:

$$\int_{\Omega} (\nabla^2 p - b) p^* \, \mathrm{d}\Omega = \int_{\Gamma 2} (q - \bar{q}) p^* \, \mathrm{d}\Gamma - \int_{\Gamma 1} (p - \bar{p}) q^* \, \mathrm{d}\Gamma \tag{25}$$

where $q = \partial p / \partial n$ and $q^* = \partial p^* / \partial n$.

Let p^* be the fundamental solution of the Laplace equation in two dimensions, represented as $p^* = -\ln r/(2\pi)$, where r is the distance from the collocation point (k) to other field points (i) given as

$$r = \sqrt{(x_k - x_i)^2 + (y_k - y_i)^2} \tag{26}$$

Copyright © 2001 John Wiley & Sons, Ltd.

Now applying Green's second identity theorem to Equation (25) and using the standard boundary element procedure [18], we can get the boundary integral equation as

$$C_i p_i + \int_\Gamma pq^* \, d\Gamma + \int_\Omega bp^* \, d\Omega = \int_\Gamma qp^* \, d\Gamma \tag{27}$$

where C_i is the Green's constant which can be calculated by surrounding the boundary point i by a small circle of radius ε and taking each term in Equation (27) in the limit as $\varepsilon \to 0$. Generally, C_i can be represented as $\theta/(2\pi)$ where θ is the internal angle at point i in radians.

In Equation (27), we have boundary integrals and domain integrals. In the present model, the domain integration is carried out by subdividing the domain into a series of internal cells, on each of which a numerical integration is performed. Here, linear elements are used for the boundary discretization and two-dimensional isoparametric quadrilateral cells are used for the internal discretization. The details of the element properties, shape functions, coordinate transformation and numerical integration used here are described in Brebbia *et al.* [18] which is not repeated here.

If the domain is discretized into M internal cells, then the domain integral can be written as

$$D_i = \int_\Omega bp^* \, d\Omega = \sum_{e=1}^{M} \left[\sum_{k=1}^{NI} w_k (bp^*)_k \right] \Omega_e \tag{28}$$

where the integral has been approximated by a summation over different cells (e varies from 1 to M), w_k are the Gauss integration weights, the function $(bp^*)_k$ needs to be evaluated at integration points k on each cell (k varies from 1 to NI, where NI is the total number of integration points on each cell) and Ω_e is the area of cell e. The term D_i is the result of the numerical integration and is different for each position i of the boundary nodes.

Assuming that the boundary of the domain is discretized into NE linear elements with N nodes, Equation (27) can be discretized and written in matrix form as

$$C_i p_i + \sum_{j=1}^{N} \bar{H}_{ij} p_j + D_i = \sum_{j=1}^{N} G_{ij} q_j \tag{29}$$

Combining the effect of the constant term C with the $\bar{H}$ matrix, we can write the matrix system as

$$Hp + D = Gq \tag{30}$$

In Equation (30), the boundary conditions are introduced and the known values are taken to the right-hand side to form a system of linear equations of the form

$$Ab = F \tag{31}$$

Copyright © 2001 John Wiley & Sons, Ltd.

where b is a vector of unknown boundary values of p and q, and F is a known vector. Equation (31) is solved using Gauss elimination scheme and all the boundary values will be then known. Once this is done, it is possible to calculate internal values of p or its derivatives. The values of p are calculated at any internal point using the Equation (27) that can be written in condensed form as

$$p_i = \int_\Gamma qp^* \, d\Gamma - \int_\Gamma pq^* \, d\Gamma - \int_\Omega bp^* \, d\Omega \tag{32}$$

The same discretization is used for the boundary integrals, that is

$$p_i = \sum_{j=1}^{N} G_{ij} q_j - \sum_{j=1}^{N} \bar{H}_{ij} p_j - D_i \tag{33}$$

where i is an internal point.

The main advantage of using BEM in the solution of the pressure Poisson equation is the effectiveness of BEM to deal with infinite domain problems. Here, only the boundary conditions of pressure on the finite computational domain are known which is used to solve the infinite domain problem.

4. COMPUTATIONAL PROCEDURE

As mentioned earlier, here an iterative scheme is used in the solution of the Navier–Stokes equations. In most of the incompressible viscous flow problems solved using Navier–Stokes equations, the most natural boundary conditions arise when the velocity is prescribed all over the boundaries of the problem. As shown in Figure 1, the boundary condition of the fixed body in the flow is set as non-slip boundary. The computational procedure adopted here includes the following iterative steps:

For the time step $n = 1$,

1. Assume at infinite domain, pressure $p = 0$ and solve the pressure Laplace equation (Equation (9)) outside the computational domain and the pressure Poisson equation (Equation (17)) inside the computational domain together and get the pressure boundary conditions on the boundaries of the computational domain.
2. Solution of the Navier–Stokes equations using three-step FEM and projection method.
   - Solve for the unknown apparent velocity values (Equation (16)).
   - Calculate the pressure distribution for the current time step from the pressure Poisson equation (17) using BEM.
   - Determine the new velocity values by solving Equation (18).
3. Check for convergence of the velocity and pressure components in the present iteration, for example

$$\frac{|p_n^{k+1} - p_n^k|}{|p_n^k|} \leq 0.0001 \quad \text{and} \quad \frac{|u_n^{k+1} - u_n^k|}{|u_n^k|} \leq 0.0001$$

Copyright © 2001 John Wiley & Sons, Ltd.

If convergence criterion is satisfied, then proceed to the next step, otherwise go to step 1.

4. In the successive time step, use the velocity and pressure components from the previous time step as initial conditions and the new boundary flow conditions and use the iterative procedure, steps 1–3. The procedure is repeated until the prescribed time step is reached.

The coefficient of drag and the coefficient of lift on the solid body are found from the following equations

$$C_{\mathrm{d}} = \frac{F_{\mathrm{d}}}{\frac{1}{2}\rho u_o^2 D}, \qquad C_{\mathrm{l}} = \frac{F_{\mathrm{l}}}{\frac{1}{2}\rho u_o^2 D} \tag{34}$$

$$F_{\mathrm{d}} = \oint_s p_s n_y \, \mathrm{d}s - \oint_s \tau_{\mathrm{s}} n_x \, \mathrm{d}s \tag{35}$$

$$F_{\mathrm{l}} = \oint_s p_s n_x \, \mathrm{d}s + \oint_s \tau_{\mathrm{s}} n_y \, \mathrm{d}s \tag{36}$$

where u_o is the fluid velocity, F_{d} is the drag force, ρ is the mass density, D is the characteristic dimension, F_{l} is the lift force, τ_{s} is the shear force acting on the body, p_s is the pressure acting on the body, and n_x and n_y are the direction cosines in the x- and y-coordinates respectively.

5. MODEL APPLICATIONS

The proposed three-step FEM–BEM model has been applied on two test problems to verify the accuracy and feasibility of the model. The present model has been used to simulate the high-Reynolds number flow past a cylinder, and also in the case of suppression of fluid forces on two circular cylinders in which one acts as a control cylinder, in the range of Reynolds number 65000 to 10^7.

5.1. High-Reynolds number flow past a single circular cylinder

Even though a large number of experimental and numerical studies have been reported on the flow across a fixed circular cylinder in the laminar flow regime [1,5,8,15,19], only a few studies have been reported on the high-Reynolds number flow across a circular cylinder [2,3,13,14]. Here, the present three-step FEM–BEM model has been applied for the simulation of high-Reynolds number flow past a fixed circular cylinder and the results are compared with the available experimental and numerical results. The present model was tested by simulating flow past a circular cylinder at a large range of Reynolds numbers of $Re = 65000$, 10^6 and 10^7. Figure 1 shows the computational domain with boundary conditions (in this case, no control cylinder). It is 20 units long (cylinder diameter is unity) and 14 units wide approximately.

Copyright © 2001 John Wiley & Sons, Ltd.

Four different meshes are used in the analysis depending on the Reynolds number. The meshes used are: mesh A, with 5568 elements and 5750 nodes; mesh B, with 4056 elements and 4186 nodes; mesh C, with 5784 elements and 5914 nodes (size of element near to the cylinder is 0.00875); mesh D, with 5784 elements and 5914 nodes (size of element near to the cylinder is 0.00027). A zoomed view of the typical mesh near to the cylinder (mesh D) is shown in Figure 2. The domain of computation was wide enough to encompass the range of the vortex shedding and fluid forces. The boundary conditions were chosen as $u = 1$, $v = 0$ at the inlet and a non-slip boundary $u = 0$, $v = 0$ on the cylinder surface. The model was run in unsteady condition.

Initially, a simulation has been performed at a high Reynolds number of 65000. For this simulation, mesh B described earlier is used and a time step of 0.02 is used. The velocity, pressure and vorticity are estimated at time $t = 200$. Figure 3(a) shows the velocity field and Figure 3(b) shows the pressure field for the Reynolds number 65000 at $t = 200$. The vorticity distribution around the cylinder is depicted in Figure 3(c). Figure 3(d) shows the streamlines for the circular cylinder. The time evolution of the coefficients of drag and lift are plotted in Figures 4 and 5 respectively. Further analysis has been carried out for flow at $Re = 10^6$ and 10^7. For the simulation with $Re = 10^6$, mesh C described earlier is used and a time step of 0.0001 is adopted. For the simulation with $Re = 10^7$, mesh D described earlier is used and a time step of 0.00001 is used. Figure 6(a)–(c) shows the pressure field, vorticity distribution and

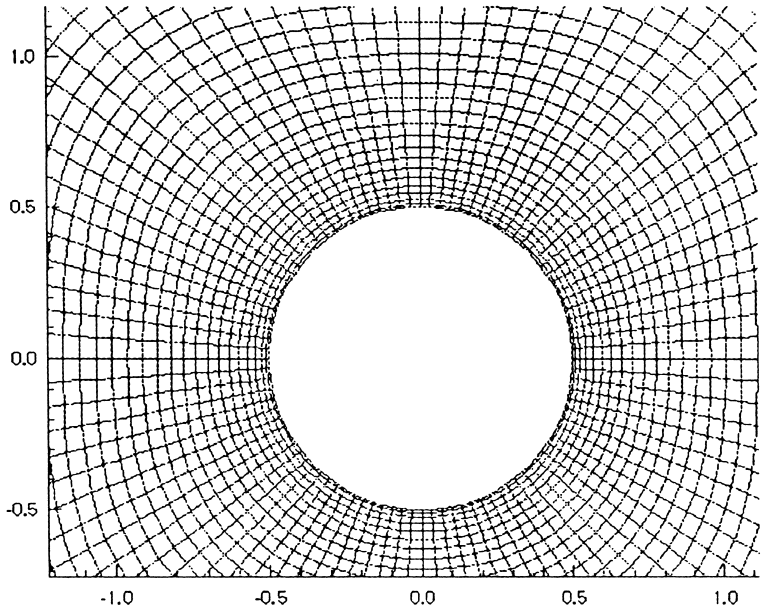

Figure 2. Zoomed view of the mesh for the computational domain—case 1.

Copyright © 2001 John Wiley & Sons, Ltd.

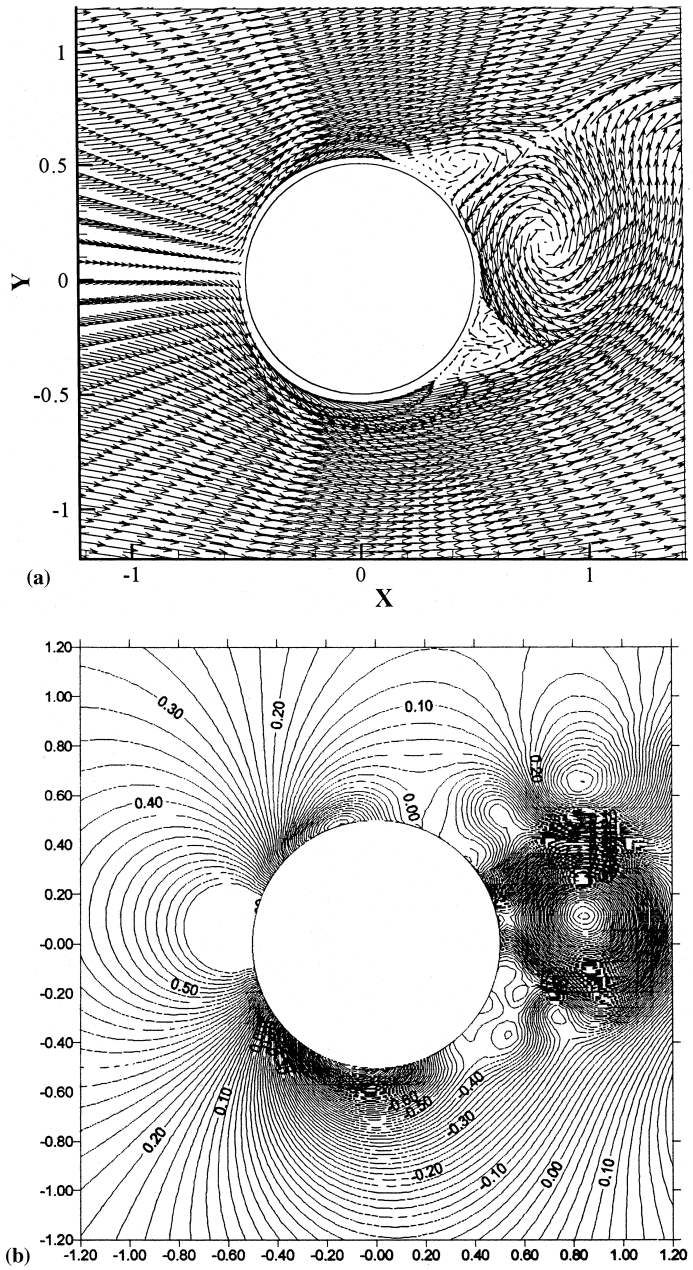

Figure 3. (a) Velocity field for flow around a circular cylinder, $Re = 6.5 \times 10^4$, $t = 200$. (b) Pressure field for flow around a circular cylinder, $Re = 6.5 \times 10^4$, $t = 200$. (c) Vorticity distribution for flow around a circular cylinder, $Re = 6.5 \times 10^4$, $t = 200$. (d) Streamline distribution for flow around a circular cylinder, $Re = 6.5 \times 10^4$, $t = 200$.

Copyright © 2001 John Wiley & Sons, Ltd.

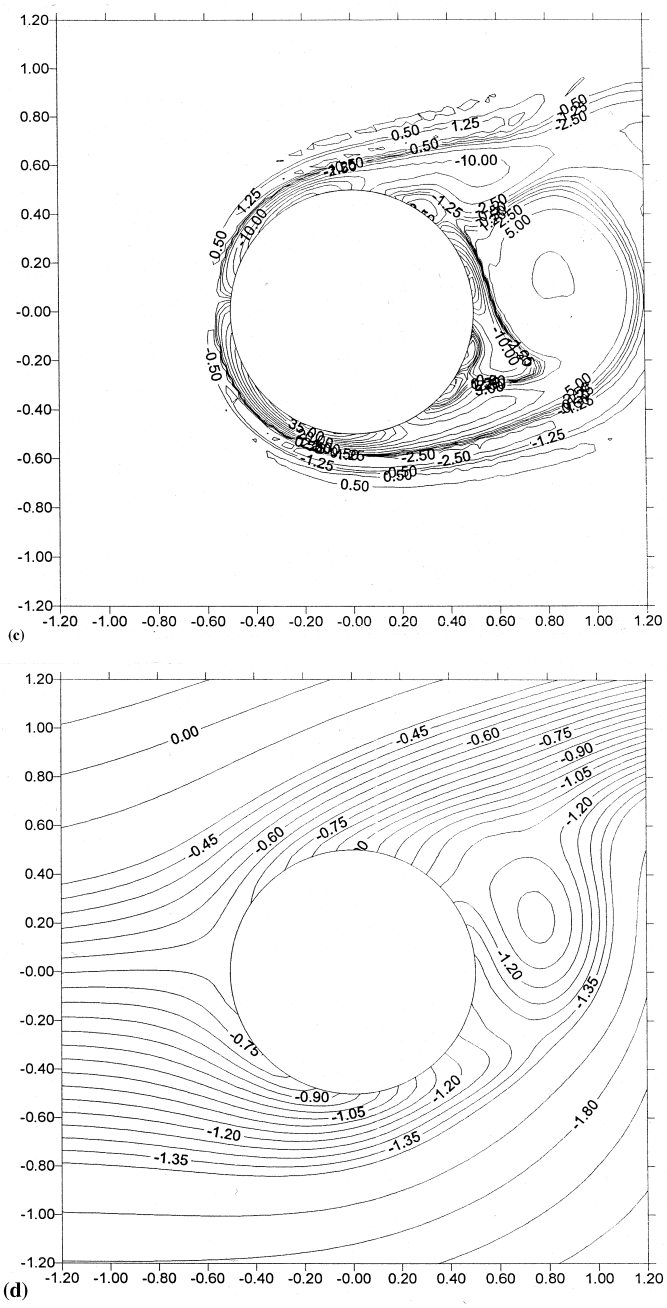

Figure 3 (*Continued*)

Copyright © 2001 John Wiley & Sons, Ltd.

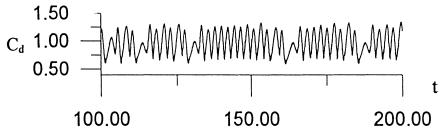

Figure 4. Time behavior of drag coefficient for flow across a circular cylinder, $Re = 6.5 \times 10^4$.

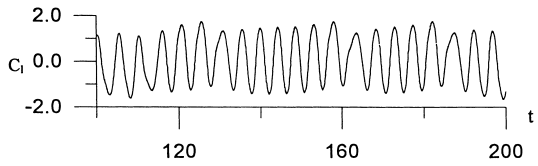

Figure 5. Time behavior of lift coefficient for flow across a circular cylinder, $Re = 6.5 \times 10^4$.

streamlines respectively for the Reynolds number 10^6 at time $t = 22$. Figure 7(a)–(c) shows the pressure field, vorticity distribution and streamlines respectively for the Reynolds number 10^7 at time $t = 0.4$. These figures clearly show the effect of increase in Reynolds number in the flow regime and the applicability of the present model to simulate flow past a circular cylinder at very high Reynolds numbers.

Figure 8 shows the variation of the coefficient of drag with respect to Reynolds numbers for various meshes mentioned earlier. The results are compared with the experimental results of Cantwell and Coles [2] and numerical results of Kakuda and Tosaka [13], Kondo [14], Tamura and Kuwahara [20] and Chang [21]. The results from the present model are generally in fairly good agreement with the other model results. The vortex shedding and fluid forces analysis in the case of the single circular cylinder is used further in the fluid force suppression analysis in the next case study by introducing a control cylinder.

For very high-Reynolds number flows past a smooth boundary such as a cylinder, the flow becomes a very interesting and challenging one, namely, the triple-deck like phenomena, as discussed by Stevertson [22] for flat plates and by Smith *et al.* [23] for smooth humps. There are three distinct decks (if we consider a cross section through the center of the cylinder), the inviscid irrotational upper deck, the inviscid rotational middle deck and the viscous rotational low deck [22]. Physically, the flow phenomena in the three decks could be analyzed by solving the potential, Euler and Navier–Stokes equations respectively. As pointed out by Smith *et al.* [23], the distinction between these three decks are rather difficult in reality. However, by using the Navier–Stokes equations solver of the present study, it is possible to observe the triple-deck like phenomena around a cylinder at very high Reynolds number. Combining Figures 6 and 7 for $Re = 10^6$ to 10^7, especially the vorticity distributions of Figures 6(b) and 7(b), and streamlines of Figures 6(c) and 7(c), the middle and lower decks are almost confined to the boundary of the cylinder, leaving the upper deck behaving like a potential flow.

Copyright © 2001 John Wiley & Sons, Ltd.

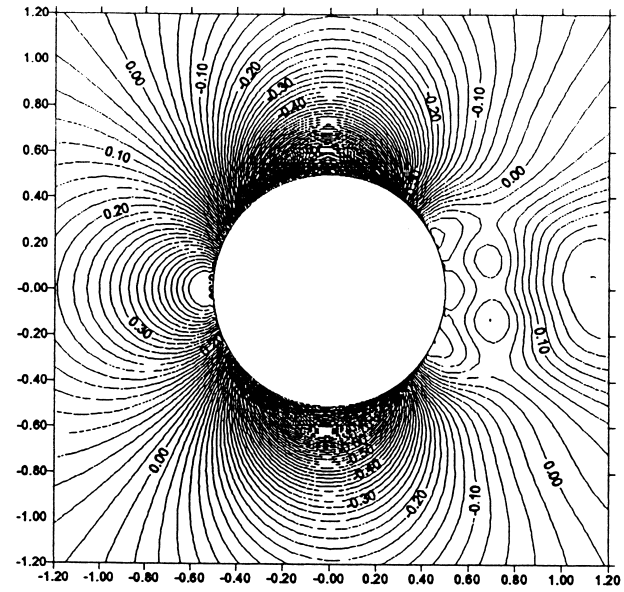

(a)

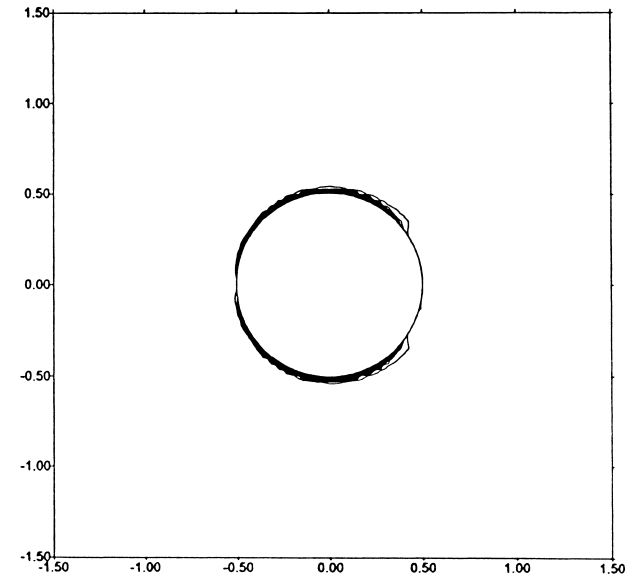

(b)

Figure 6. (a) Pressure field for flow around a circular cylinder, $Re = 10^6$, $t = 22$. (b) Vorticity distribution for flow around a circular cylinder, $Re = 10^6$, $t = 22$. (c) Streamline distribution for flow around a circular cylinder, $Re = 10^6$, $t = 22$.

Copyright © 2001 John Wiley & Sons, Ltd.

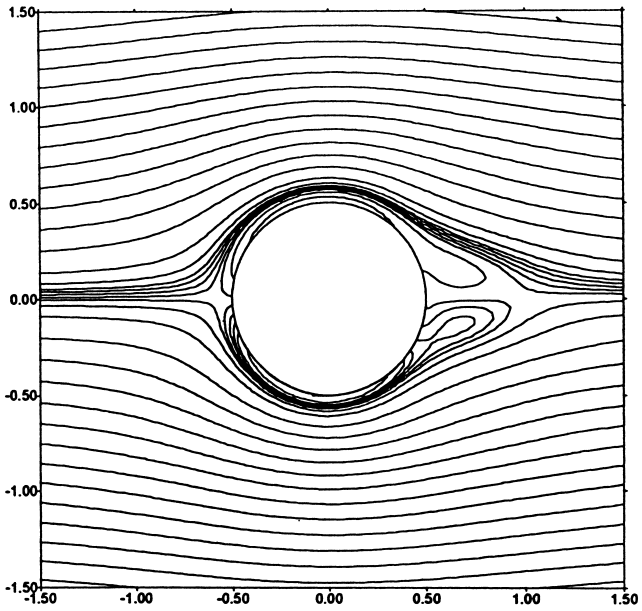

(c)

Figure 6 (*Continued*)

5.2. Suppression of flow past a circular cylinder with a control cylinder at high Reynolds numbers

In this case study, the model is applied to investigate the effect of a control cylinder in the vicinity of a main circular cylinder in a uniform flow field, which suppresses the fluid forces by the main circular cylinder. Recently, Sakamoto and Haniu [3] showed experimentally that the vortex shedding behind a circular cylinder can be suppressed at high Reynolds numbers using an appropriately placed small control cylinder. In this case study, the vortex alteration and suppression are investigated numerically using the three-step FEM–BEM model at a high Reynolds number of 65000.

Here, the same problem described in previous case study (Section 5.1) is used but a small circular cylinder (of size $d/D = 0.06$, where D is the diameter of the main cylinder and d is the diameter of the control cylinder) is placed at various positions, and its effects on the fluid forces on the main cylinder are numerically analyzed. A sample of zoomed discretization near the circular cylinders with the main cylinder and control cylinder is shown in Figure 9. The domain is discretized using 4060 elements and 4193 nodes. Figure 10 shows the definition of the coordinate system used in the present study. The control cylinder is placed at a position of $G/d = 2$ (refer to Figure 10) above the middle centerline of the main cylinder with α angles (0°–180°) and its effect on the fluid flow at an interval of 15° is investigated. The diameter of the control cylinder and the G/d position are chosen according to the values used by Sakamoto and Hainu [3].

Copyright © 2001 John Wiley & Sons, Ltd.

Initially, the effect of the control cylinder placed at 30° is analyzed. The velocity, pressure and vorticity of the main cylinder in the presence of the control cylinder are estimated at time $t = 200$ ($\Delta t = 0.02$). Figure 11(a) shows the velocity field and Figure 11(b) depicts the pressure field at time $t = 200$. The vorticity distribution around the cylinder is depicted in Figure 11(c). Figure 11(d) shows the streamlines for the circular cylinder. These figures show the salient features of the effect of the control cylinder in the flow regime of the main circular cylinder in comparison with the flow field described in the first case (Section 5.1). From these figures, it can be easily observed that there is a significant change in the vortex shedding and fluid forces due to the influence of the control cylinder.

To investigate the effects of various positions of the control cylinder on the vortex shedding for the selected size of the control cylinder and $G/d = 2$, numerical analyses have been carried out by placing the control cylinder at various positions. Figure 12(a)–(d) shows the velocity field, pressure distribution, vorticity distribution and streamlines for a 45° position of the control cylinder at time $t = 70$ ($\Delta t = 0.005$). Figure 13 illustrates the pressure distribution for a 90° position of the cylinder at time $t = 100$ ($\Delta t = 0.01$). Figure 14(a)–(d) exhibits the velocity field, pressure distribution, vorticity distribution and stream lines for a 120° position of the control cylinder at time $t = 100$ ($\Delta t = 0.01$), and Figure 15 shows the pressure distribution for

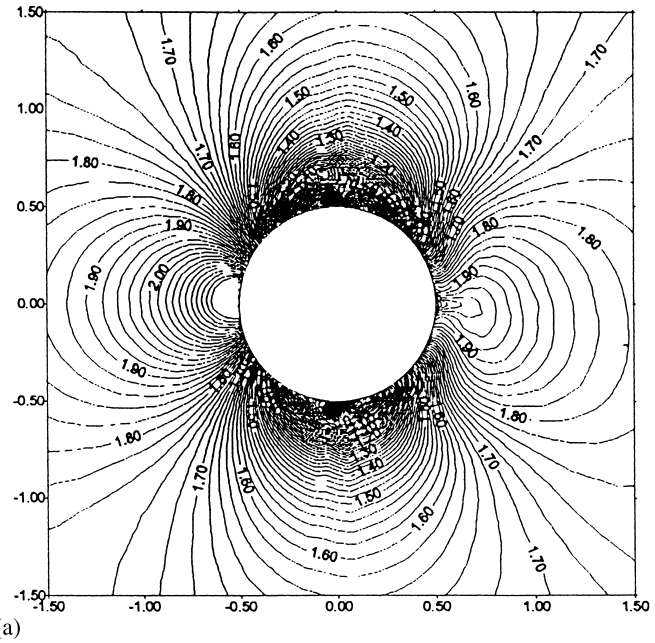

(a)

Figure 7. (a) Pressure field for flow around a circular cylinder, $Re = 10^7$, $t = 0.4$. (b) Vorticity distribution for flow around a circular cylinder, $Re = 10^7$, $t = 0.4$. (c) Streamline distribution for flow around a circular cylinder, $Re = 10^7$, $t = 0.4$.

Copyright © 2001 John Wiley & Sons, Ltd.

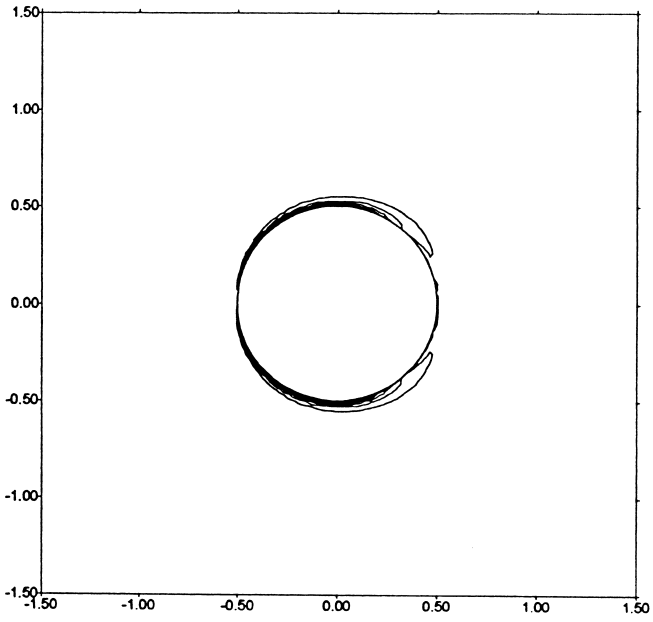

(b)

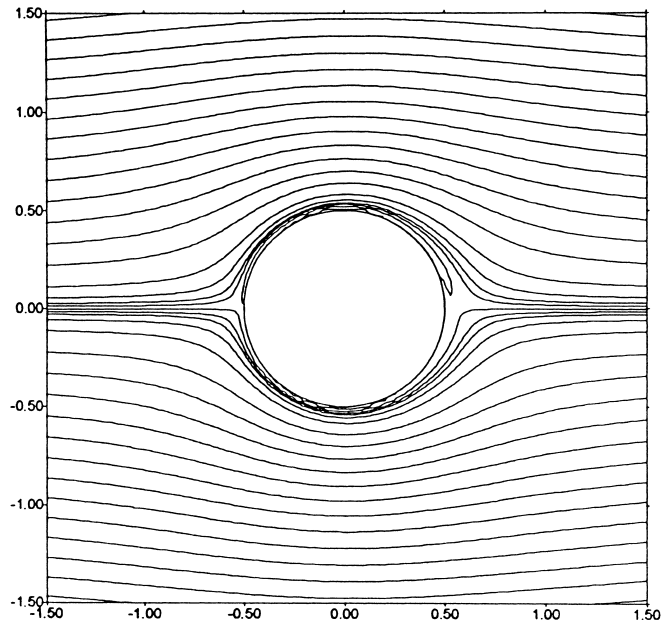

(c)

Figure 7 (*Continued*)

Copyright © 2001 John Wiley & Sons, Ltd.

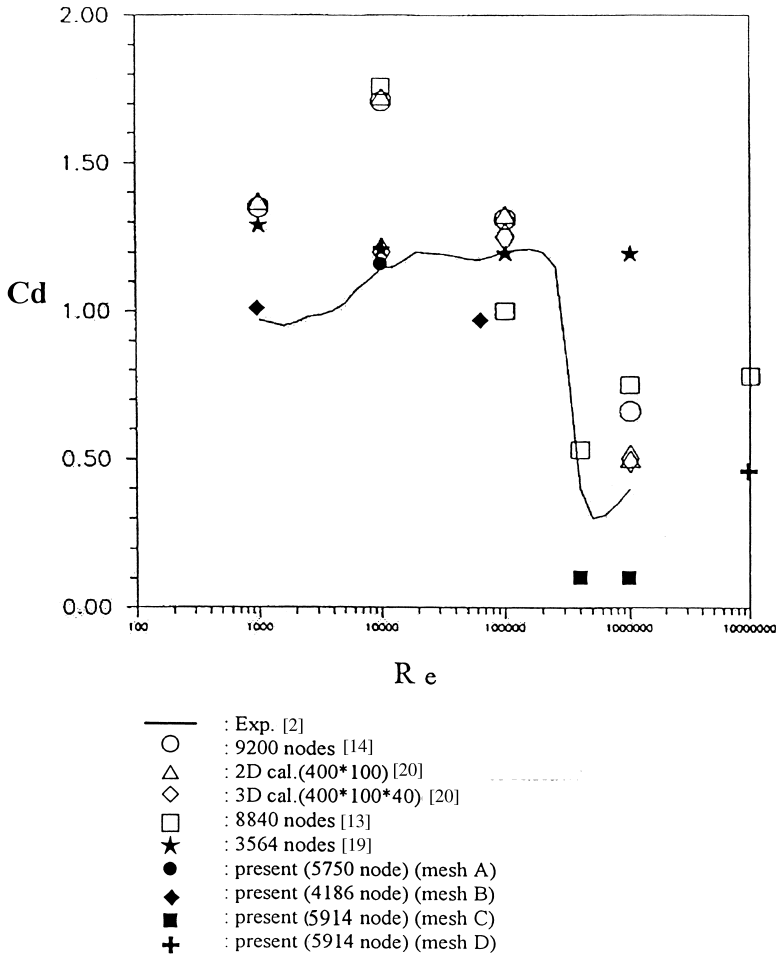

Figure 8. Drag coefficient variation with reference to Reynolds number.

a 150° position of the control cylinder at time $t = 100$ ($\Delta t = 0.01$). It is very clear that the vortex-shedding pattern considerably changes with the variation in the position of the control cylinder.

The method of quantifying the changes in fluid forces occurring due to the introduction of the control cylinder in the wake is by monitoring the drag and lift forces on the main cylinder. Figure 16 shows the ratio of coefficient of drag (C_{dc}) due to the control cylinder to the drag coefficient (C_{dn}) without the control cylinder for various positions of the control cylinder. Figure 17 shows the ratio of the root mean square (r.m.s.) value of the coefficient of lift (C_{lfc})

Copyright © 2001 John Wiley & Sons, Ltd.

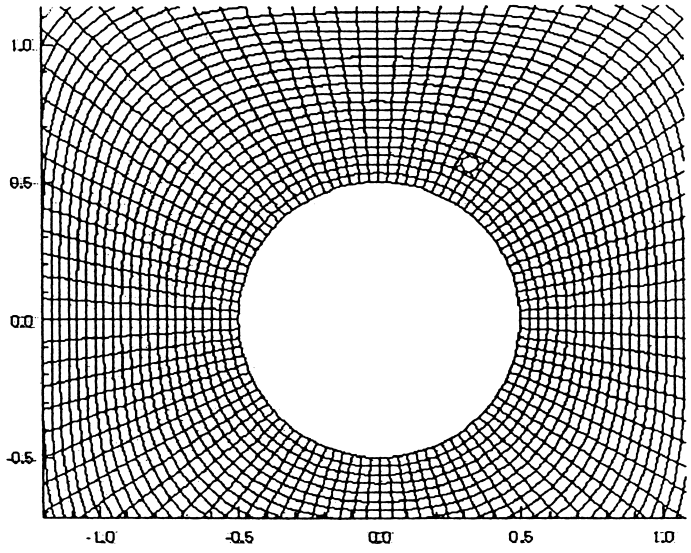

Figure 9. Zoomed view of the mesh for the computational domain—case 2.

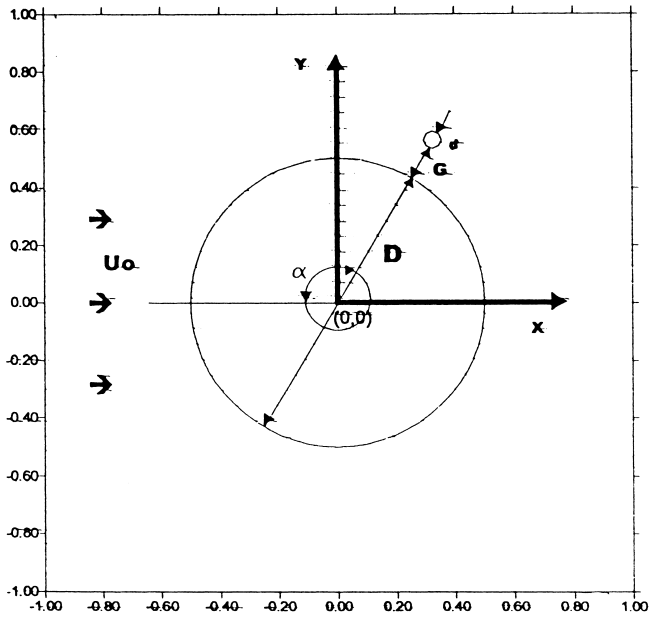

Figure 10. Definition sketch and coordinate position of the main and control cylinders.

Copyright © 2001 John Wiley & Sons, Ltd.

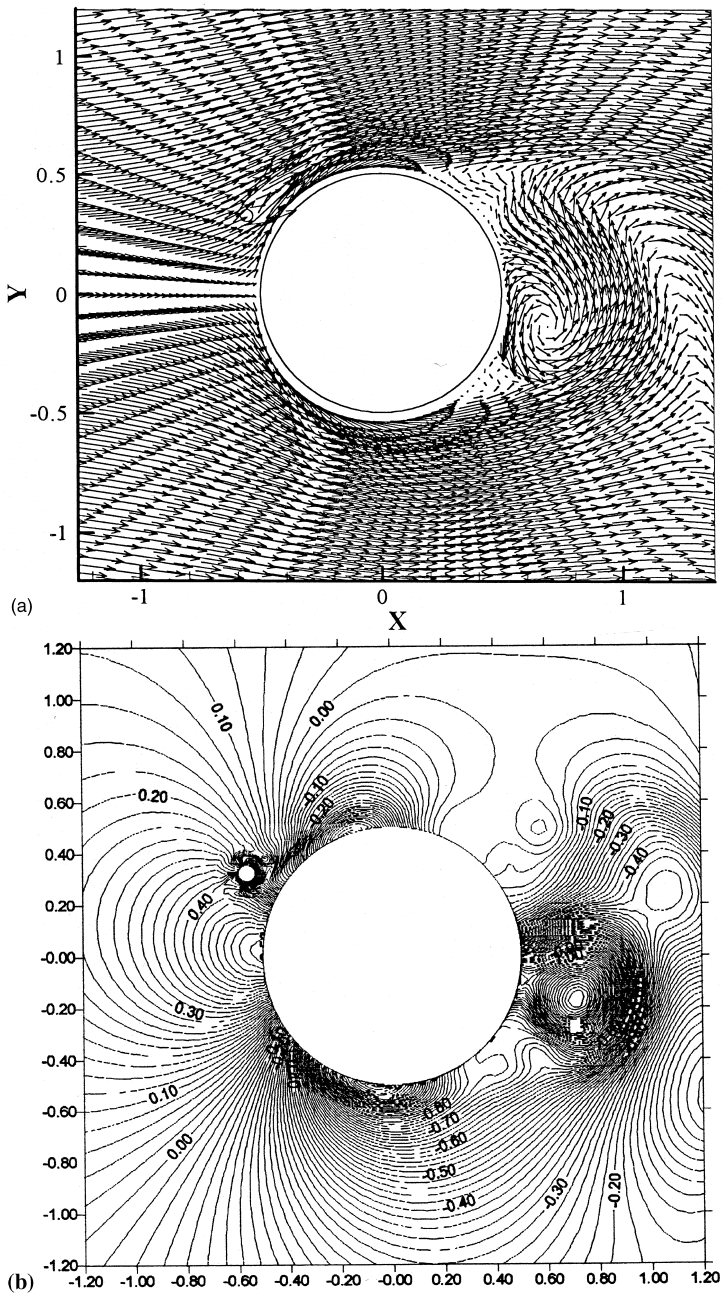

Figure 11. (a) Velocity field for flow around a circular cylinder with control cylinder, $Re = 6.5 \times 10^4$, $t = 200$, $\alpha = 30°$. (b) Pressure field for flow around a circular cylinder with control cylinder, $Re = 6.5 \times 10^4$, $t = 200$, $\alpha = 30°$. (c) Vorticity distribution for flow around a circular cylinder with control cylinder, $Re = 6.5 \times 10^4$, $t = 200$, $\alpha = 30°$. (d) Streamline distribution for flow around a circular cylinder with control cylinder, $Re = 6.5 \times 10^4$, $t = 200$, $\alpha = 30°$.

Copyright © 2001 John Wiley & Sons, Ltd.

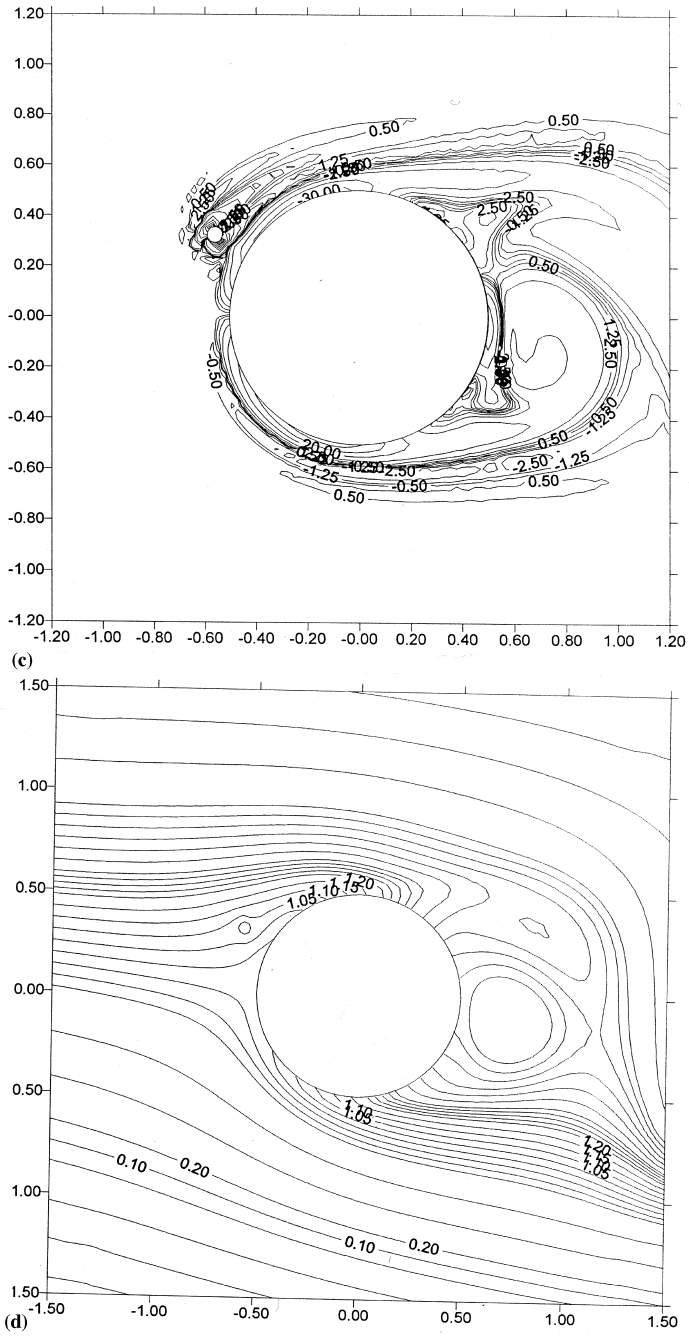

Figure 11 (*Continued*)

Copyright © 2001 John Wiley & Sons, Ltd.

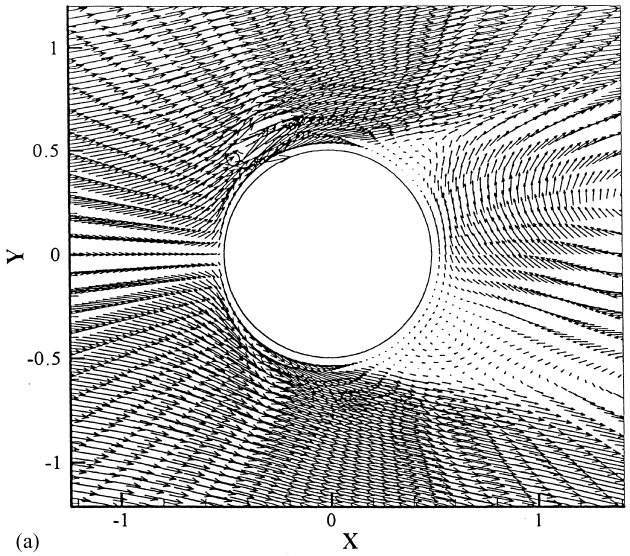

(a)

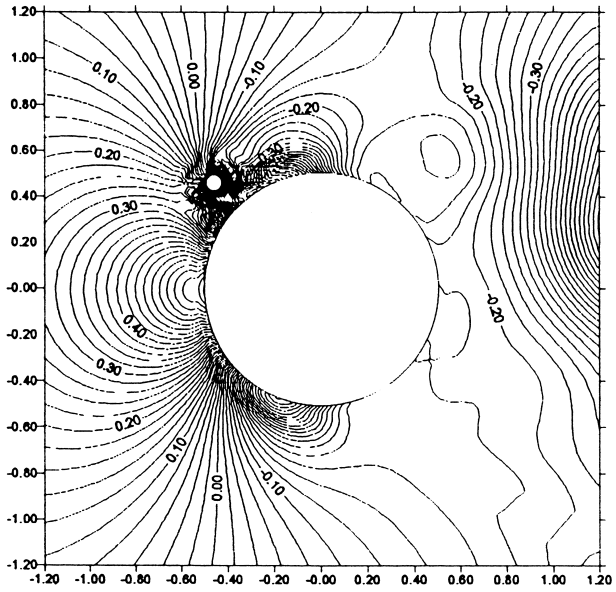

(b)

Figure 12. (a) Velocity field for flow around a circular cylinder with control cylinder, $Re = 6.5 \times 10^4$, $t = 70$, $\alpha = 45°$. (b) Pressure field for flow around a circular cylinder with control cylinder, $Re = 6.5 \times 10^4$, $t = 70$, $\alpha = 45°$. (c) Vorticity distribution for flow around a circular cylinder with control cylinder, $Re = 6.5 \times 10^4$, $t = 70$, $\alpha = 45°$. (d) Streamline distribution for flow around a circular cylinder with control cylinder, $Re = 6.5 \times 10^4$, $t = 70$, $\alpha = 45°$.

Copyright © 2001 John Wiley & Sons, Ltd.

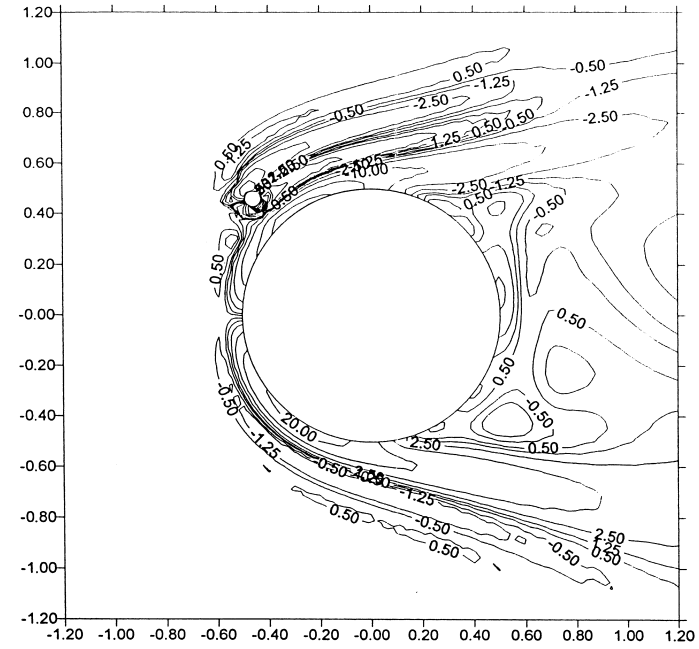

(c)

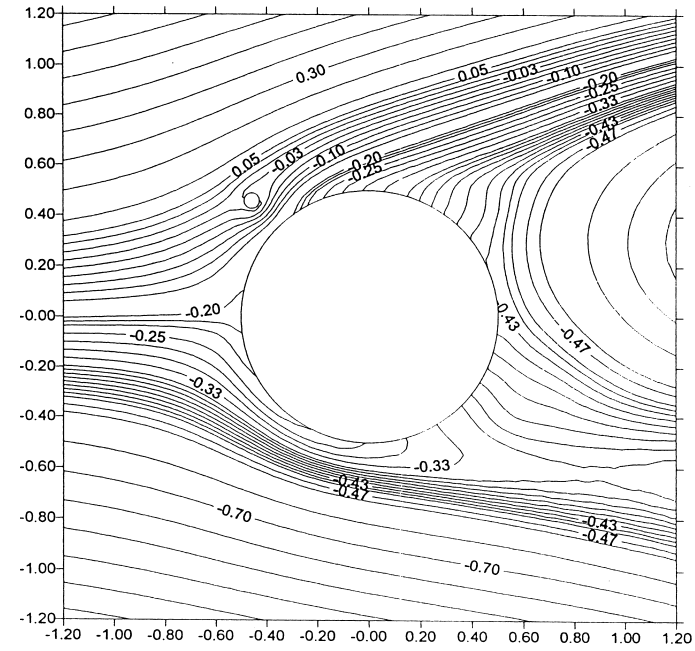

(d)

Figure 12 (*Continued*)

Copyright © 2001 John Wiley & Sons, Ltd.

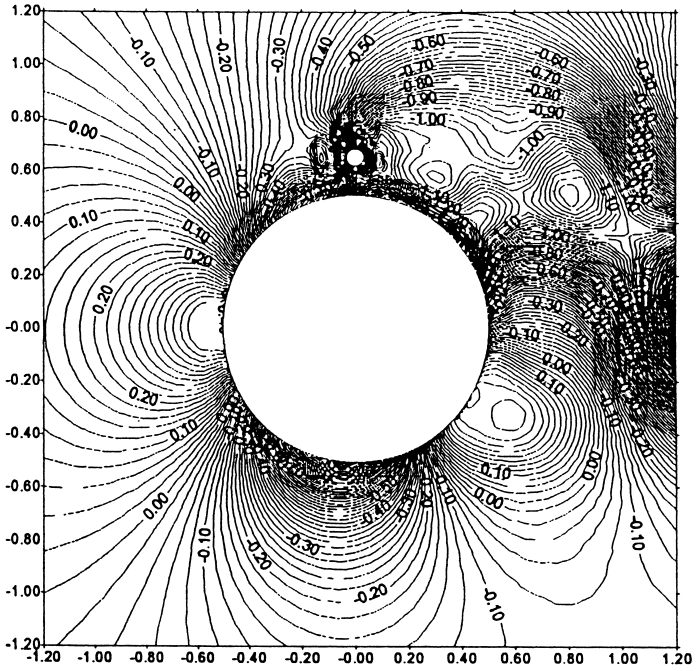

Figure 13. Pressure field for flow around a circular cylinder with control cylinder, $Re = 6.5 \times 10^4$, $t = 100$, $\alpha = 90°$.

due to the control cylinder to the lift coefficient (C_{lfn}) without the control cylinder for the various positions of the control cylinder. The results are compared with the experimental results of Sakamoto and Haniu [3] as well as Chang [19]. The experimental investigation of Sakamoto and Haniu [3] reported that the critical position for the control cylinder to suppress the fluid forces is near 60° and near 120°. However, the numerical simulations of the present study indicate a slightly different value of near 50° and near 120°. This difference may be attributed to the differences of the level of disturbance, specific end conditions and three-dimensional effects.

Figures 18 and 19 show respectively the coefficients of drag and lift calculated with reference to the various positions of the control cylinder. Figure 20 displays the corresponding power spectrum of the fluctuating drag coefficient for various positions of the control cylinder. These figures clearly depict the effect of the control cylinder in the flow regime in comparison to the case without the control cylinder. The coefficients of drag and lift drastically change with the position of the control cylinder. As is obvious, large reductions in the time-averaged drag is due to the displacement of the separation points, which are very conspicuous in the cases of $\alpha = 45°$ and 120°.

Copyright © 2001 John Wiley & Sons, Ltd.

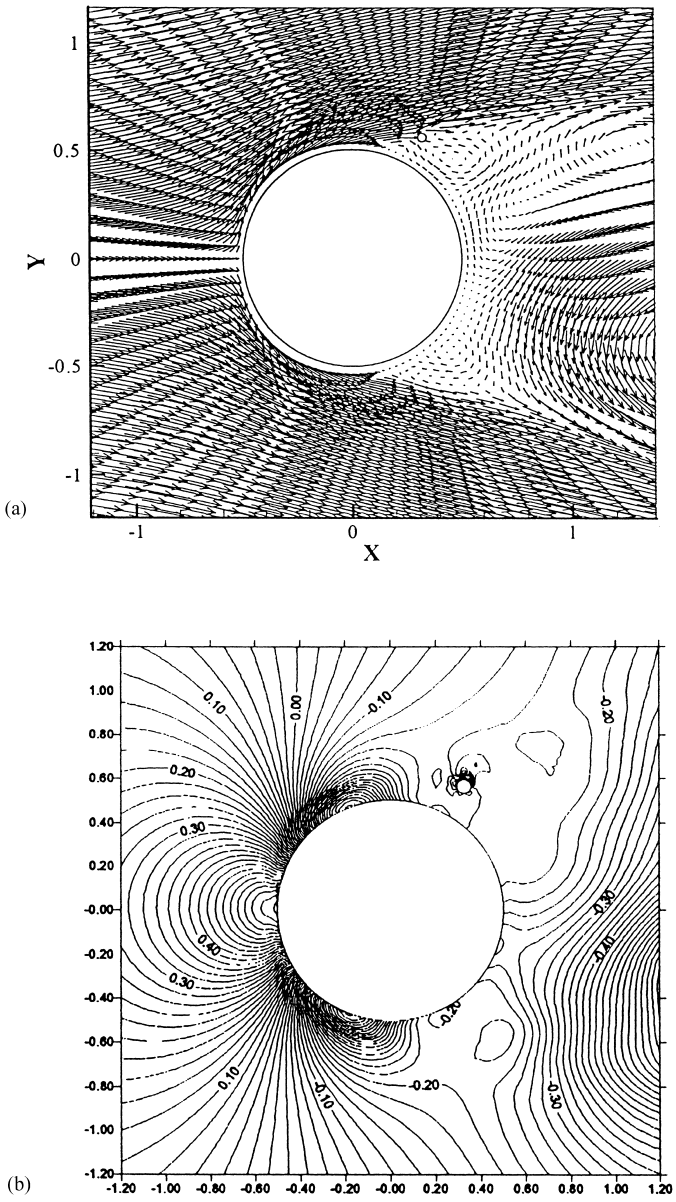

Figure 14. (a) Velocity field for flow around a circular cylinder with control cylinder, $Re = 6.5 \times 10^4$, $t = 100$, $\alpha = 120°$. (b) Pressure field for flow around a circular cylinder with control cylinder, $Re = 6.5 \times 10^4$, $t = 100$, $\alpha = 120°$. (c) Vorticity distribution for flow around a circular cylinder with control cylinder, $Re = 6.5 \times 10^4$, $t = 100$, $\alpha = 120°$. (d) Streamline distribution for flow around a circular cylinder with control cylinder, $Re = 6.5 \times 10^4$, $t = 100$, $\alpha = 120°$.

Copyright © 2001 John Wiley & Sons, Ltd.

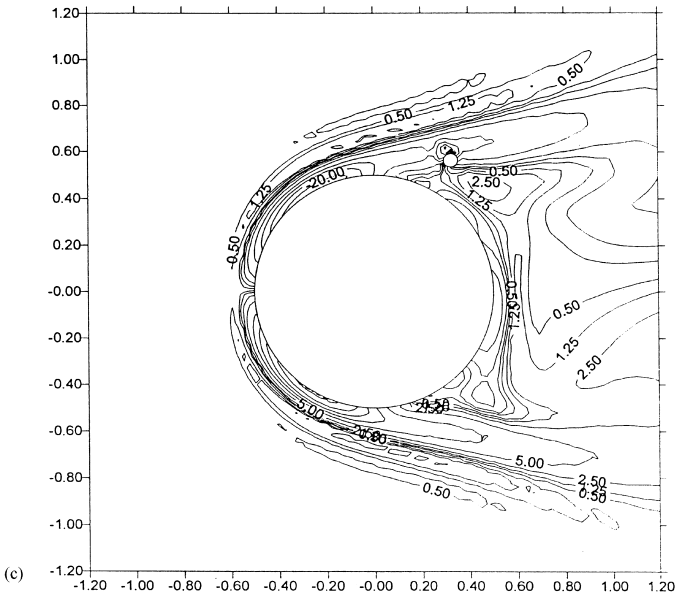

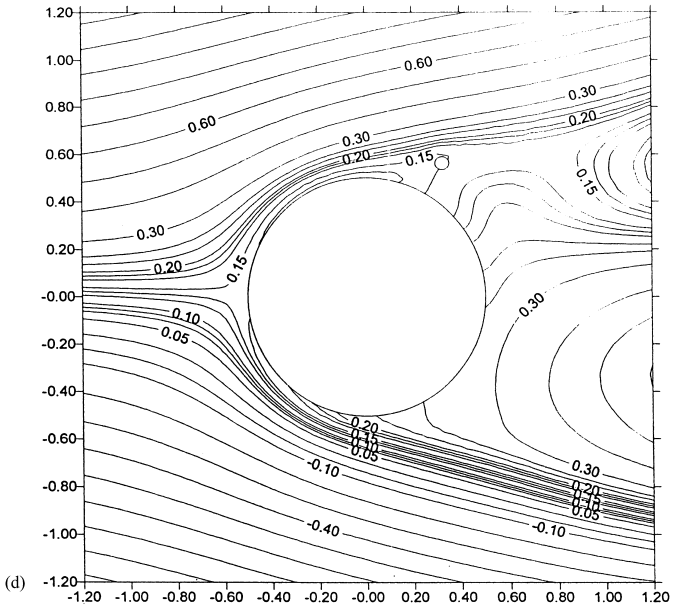

Figure 14 (*Continued*)

Copyright © 2001 John Wiley & Sons, Ltd.

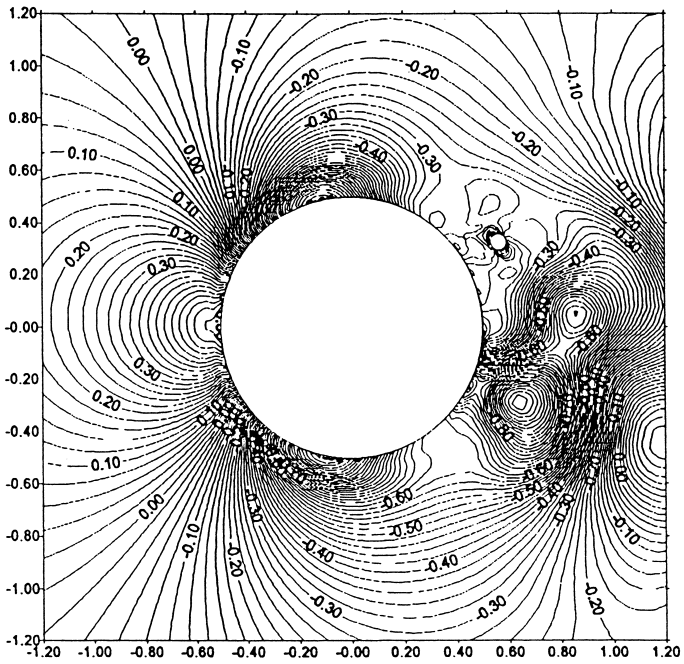

Figure 15. Pressure field for flow around a circular cylinder with control cylinder, $Re = 6.5 \times 10^4$, $t = 100$, $\alpha = 150°$.

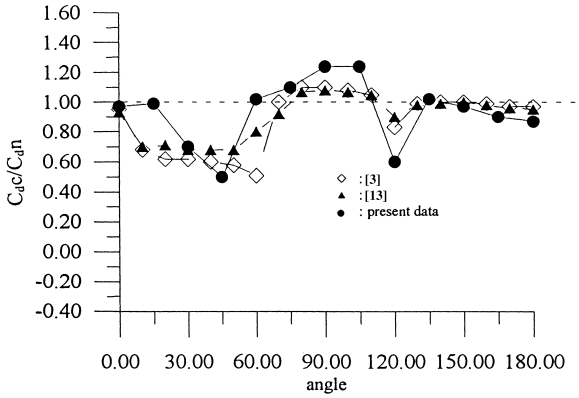

Figure 16. Comparison of the ratio of drag coefficient of cylinder with and without control cylinder for various α angles.

Copyright © 2001 John Wiley & Sons, Ltd.

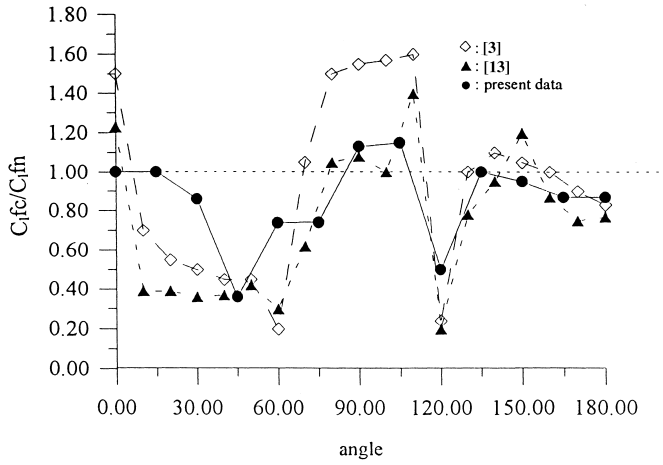

Figure 17. Comparison of the ratio of r.m.s. value of lift coefficient of cylinder with and without control cylinder for various α angles.

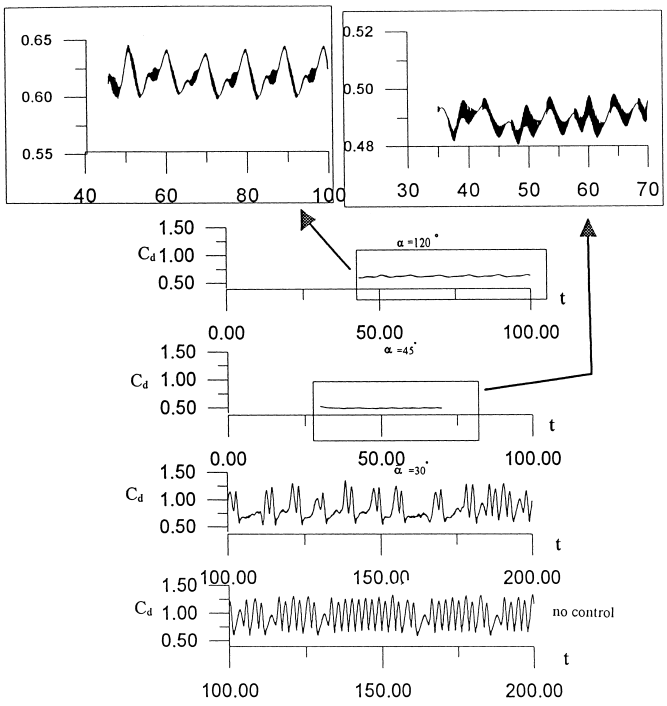

Figure 18. Drag coefficient of cylinder with and without control cylinder for various α angles.

Copyright © 2001 John Wiley & Sons, Ltd.

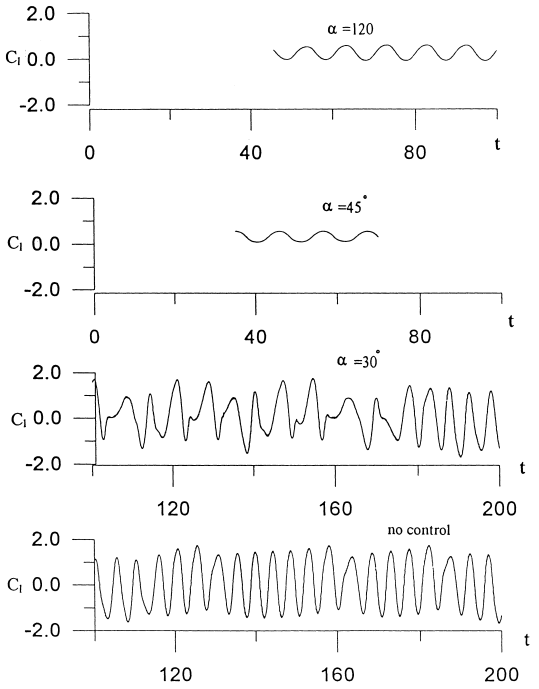

Figure 19. Lift coefficient of cylinder with and without control cylinder for various α angles.

This numerical study further explains the study of Sakamato and Haniu [3] on the effects of a small control cylinder, in the wake of a main circular cylinder at a high Reynolds number. The pressure fields and vorticity distributions plotted reveal that the presence of the smaller cylinder reduces the growth rate of the disturbances and its suppression accompanied by the disappearance of the sharp spectral peaks, coincides with negative temporal growth rates. The presence of the control cylinder alters the stability of the flow and diverts small amounts of fluid into the wake of the main cylinder. The position and size of the control cylinder are very important factors in the vortex shedding and suppression, for the given Reynolds number of the flow regime [3], even though in the present analysis the effect of the size of the control cylinder is not considered.

The reasons for the suppression of fluid forces by the proper placement of a small control cylinder in the near wake of the main cylinder, are attributed to the redistribution of the vorticity in the shear layer, the fluid diversion between main and control cylinders to reduce the velocity gradients, as well as the pressure change between the two cylinders, as pointed out by Sakamoto and Haniu [3]. Figures 3(c), 12(c) (at 45°) and 14(c) (at 120°) respectively show the vorticity distributions without the control cylinder and with the

Copyright © 2001 John Wiley & Sons, Ltd.

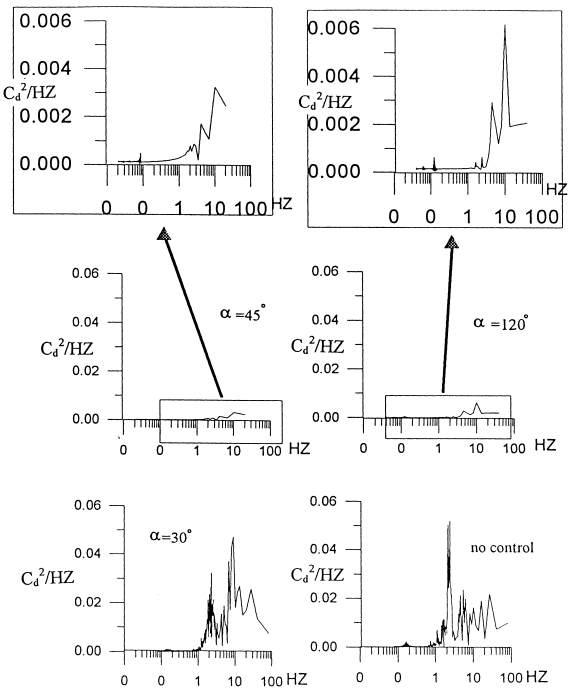

Figure 20. Power spectrum of fluctuating drag coefficient of cylinder with and without control cylinder for various α angles.

control cylinder at $Re = 65000$. The concentrated vorticity in the shear layer behind the main cylinder is smeared and diffused by the proper placement of the control cylinder. The suppression of vortex shedding as a consequence will reduce the magnitudes of the drag and lift forces as well as the oscillating frequencies. The pressure distributions without the control cylinder and with the control cylinder are shown for comparison in Figures 3(b), 12(b) (at 45°) and 14(b) (at 120°) respectively. The drastic reduction of pressure in the wake of the main cylinder by the introduction of the control cylinder suggests the mechanism for the suppression of vortex shedding and fluid forces.

6. CONCLUDING REMARKS

In this paper a novel computational model is presented to solve high-Reynolds number incompressible viscous flow problems. In the model, the transient Navier–Stokes equations in primitive variables are solved by a three-step FEM using a projection method, and the Poisson type pressure equations are solved using BEM. By coupling the three-step FEM

Copyright © 2001 John Wiley & Sons, Ltd.

and BEM, the model is able to handle infinite domain problems efficiently. The infinite boundary value problems are solved by extracting the boundary effects on a specified finite computational domain using the projection method.

The present model is applied to simulate high-Reynolds number flow past a single circular cylinder, and flow past two cylinders in which one acts as a control cylinder. The simulation results are compared with some experimental data and other numerical models and found to be feasible and satisfactory. Even though two-dimensional problems are presented here, the model can be easily extended to three-dimensional problems and also turbulence models can be incorporated.

REFERENCES

1. Strykowski PJ, Sreenivasan KR. On the formation and suppression of vortex shedding at low Reynolds numbers. *Journal of Fluid Mechanics* 1990; **218**: 71–107.
2. Cantwell B, Coles D. A experimental study of entrainment and transport in the turbulent near wake of a circular cylinder. *Journal of Fluid Mechanics* 1983; **136**: 321–374.
3. Sakamoto H, Haniu H. Optimum suppression of fluid forces acting on a circular cylinder. *Journal of Fluids Engineering*, *Transactions of ASME* 1994; **116**: 221–227.
4. Zdravkovich MM. Review and classification of various aerodynamic and hydrodynamic means for suppressing vortex shedding. *Journal of Wind Engineering and Industrial Aerodynamics* 1981; **7**(2): 145–189.
5. Braza M, Chassaing P, Minh HH. Numerical study and physical analysis of the pressure and velocity fields in the near wake of a circular cylinder. *Journal of Fluid Mechanics* 1986; **165**: 79–139.
6. Franke R, Rodi W, Schonung B. Numerical calculation of laminar vortex shedding flow past cylinders. *Journal of Wind Engineering and Industrial Aerodynamics* 1990; **35**: 237–257.
7. Lecointe Y, Piquet J. Flow structure in the wake of an oscillating cylinder. *Journal of Fluids Engineering*, *Transactions of ASME* 1989; **111**: 139–148.
8. Jackson CP. A finite-element study of the onset of vortex shedding in flow past variously shaped bodies. *Journal of Fluid Mechanics* 1987; **182**: 23–45.
9. Reddy JN. *Finite Element Method*. McGraw-Hill: New York, 1993.
10. Taylor C, Hughes TG. *Finite Element Programming of The Navier–Stokes Equations*. Pineridge Press Limited: Swansea, 1981.
11. Power H, Wrobel LC. *Boundary Integral Methods in Fluid Mechanics*. Computational Mechanics Publications: Southampton, 1995.
12. Brooks A, Hughes TJR. Streamline upwind/Petrov–Galerkin formulations for convection dominated flow with particular emphasis on the incompressible Navier–Stokes equations. *Computer Methods in Applied Mechanics and Engineering* 1982; **32**: 199–259.
13. Kakuda K, Tosaka N. Numerical simulation of high Reynolds number flows by Petrov–Galerkin finite element method. *Journal of Wind Engineering and Industrial Aerodynamics* 1993; **46/47**: 339–347.
14. Kondo N. Direct third-order upwind finite element simulation of high Reynolds number flows around a circular cylinder. *Journal of Wind Engineering and Industrial Aerodynamics* 1993; **46/47**: 349–356.
15. Donea JA. Taylor–Galerkin method for convective transport problems. *International Journal for Numerical Methods in Fluids* 1984; **20**: 101–119.
16. Jiang CB, Kawahara M. The analysis of unsteady incompressible flows by a three-step finite element method. *International Journal for Numerical Methods in Fluids* 1993; **16**: 793–811.
17. Young DL, Liao CB, Sheen HJ. Computations of recirculation zones of a confined annular swirling flow. *International Journal for Numerical Methods in Fluids* 1999; **29**: 791–810.
18. Brebbia CA, Telles JCF, Wrobel LC. *Boundary Element Techniques—Theory and Applications in Engineering*. Springer-Verlag: Berlin, 1984.
19. Chang YC. Experimental investigations on the control of vortex shedding behind a circular cylinder. MS thesis, Institute of Applied Mechanics, National Taiwan University, 1996.
20. Tamura T, Kuwahara K. Direct finite difference computation of turbulent flow around a circular cylinder. *Numerical Methods in Fluid Dynamics* 1989; **2**: 645–650.

Copyright © 2001 John Wiley & Sons, Ltd.

21. Chang JT. Numerical simulation of wind flows over structures. PhD thesis, Graduate Institute of Civil Engineering, National Taiwan University, 1995.
22. Stewartson K. Multi-structured boundary layers on flat plates and related bodies. In *Advances in Applied Mechanics*, vol. 14, Yih CS (ed.). Academic Press: New York, 1974; 146–239.
23. Smith FT, Brighton PWM, Jackson PS, Hunt JCR. On boundary-layer flow past two-dimensional obstacles. *Journal of Fluid Mechanics* 1981; **113**: 123–152.

Copyright © 2001 John Wiley & Sons, Ltd.